International Journal of Rock Mechanics & Mining Sciences 47 (2010) 1104–1113

Poroelastic contribution to the reservoir stress path

Johannes B. Altmann [a,*], Tobias M. Müller [b], Birgit I. R. Müller [a], Mark R. P. Tingay [c], Oliver Heidbach [d]

[a] *Geophysical Institute, University of Karlsruhe, Hertzstraße 16, 76187 Karlsruhe, Germany*
[b] *CSIRO CESRE, Australian Resources Research Centre, 26 Dick Perry Avenue, Kensington WA 6151, Australia*
c Australian School of Petroleum Science, University of Adelaide, Australia
[d] *Helmholtz Centre Potsdam - GFZ German Research Centre for Geosciences, Telegrafenberg, 14473 Potsdam, Germany*

ARTICLE INFO

Article history:
Received 13 August 2009
Received in revised form 2 July 2010
Accepted 5 August 2010
Available online 21 August 2010

Keywords:
Pore pressure/stress coupling
Reservoir
Injection
Depletion
Numerical modelling

ABSTRACT

Pore pressure/stress coupling is the change in the smaller horizontal stress σ_h associated with changes in pore pressure P, and has been measured in numerous reservoirs worldwide. These measurements suggest that the change in minimum horizontal stress $\Delta\sigma_h$ is on average ca. 64% of the change in the reservoir pore pressure ΔP, but can be as low as 34% and as high as 118%. Conventionally it is assumed that the total vertical stress σ_v, given by the overburden, is not affected by changes in pore pressure, in contrast to the horizontal stresses σ_H and σ_h. We investigate analytically and numerically the spatio-temporal pore pressure and stress evolution in poroelastic media for continuous fluid injection at a point source, and calculate from the numerical modelling results the ratio $\Delta\sigma/\Delta P$. Analytically, we show that the measured average of $\Delta\sigma_h/\Delta P$ can mathematically be deduced from the long-term limit of the spatio-temporal evolution of pore pressure and horizontal stress caused by fluid injection at a point source. We compare our numerical results to the analytical solution for continuous point injection into homogeneous poroelastic media as well as to $\Delta\sigma_h/\Delta P$ values measured in the field, and show that all stress components change with a variation in P. We use the concept of poroelasticity to explain the observed coupling between pore pressure and stress in reservoirs, and we consider different measurement locations and measurement times as one possible reason for the measured variation in $\Delta\sigma_h/\Delta P$ in different oil fields worldwide.

1. Introduction

Pore pressure changes in reservoirs cause deformation processes and changes in the total stress within the reservoir and in its surroundings due to the coupling between pore pressure and stress [1]. Hillis [1] and Addis [2] differentiate between overpressure-related basin-scale and depletion-related field-scale coupling of pore pressure and stress. The relation between virgin stress and pore pressure data for the Gulf Coast region, Venezuela, Brunei, etc., has been reviewed in [3], and regional relationships between horizontal stress and pore pressure have been derived for normally and abnormally pressured formations. The measurements indicate that the minimum horizontal stress increases from shallow normally pressured reservoirs to deeper overpressured sequences of sedimentary basins over geological timescales. During fluid injection into reservoirs or depletion from reservoirs pressure perturbations occur. Repeated measurements of stress and pore pressure during the depletion of oil fields show that changes in pore pressure P and minimum horizontal stress σ_H are coupled, e.g. for Texas [4] or the North Sea [5,6].

In this paper we consider the field-scale coupling between pore pressure and stresses, which is depletion/injection related. Santarelli et al. [7] point out the importance of changes in pressure during depletion known as the reservoir stress path, which is essential for sand production, mud losses, hydraulic fracturing or wellbore stability in overpressured sequences with a narrow window between fracturing gradient and formation pressure. Hillis [8] or Tingay et al. [9] call the phenomenon of depletion-induced reduction of P in hydrocarbon reservoirs leading to a decrease in σ_h ''pore pressure/stress coupling'', abbreviated in the following as PSC, and also known as stress depletion response of the reservoir [2,4]. The strength of the PSC can be expressed by the ratio $\Delta\sigma_h/\Delta P$, which describes the change in total minimum horizontal stress caused by a change in pore pressure. Worldwide stress and pore pressure measurements indicate that the ratio $\Delta\sigma_h/\Delta P$ is not a constant value, but can vary between 0.34 and 1.18, with an average of 0.64 (Table 1). One might argue that $\Delta\sigma_h/\Delta P$ values range from one reservoir to another, but the ratio varies also inside the reservoirs, e.g. the Valhall reservoir in the North Sea [5,6,10]. Zoback and Zinke [10] investigated the pore pressure drawdown at the Tor formation of the Valhall field. They differentiate between well locations in the crest and in the flank of the reservoir. In this case $\Delta\sigma_h/\Delta P$ increases from 0.70 (crest) to 0.84 (flank).

Numerical models with uniform prescribed depletion of pore pressure show that part of the weight of the overburden is transferred to the formations at the sides of the reservoir (stress arching), leading to higher risk for failure [14,15]. The deformation associated with the coupled changes of P and stress affect rock properties such as acoustic wave velocity, bulk density, porosity and permeability that may lead to modifications of reservoir fluid flow, reactivation of reservoir-sealing faults, failure of the caprock or

* Corresponding author. Tel.: +49 721 608 4427; fax: +49 721 711 73.
E-mail address: johannes.altmann@gpi.uni-karlsruhe.de (J.B. Altmann)

Table 1
Basin-scale and field-scale values for $\Delta\sigma_h/\Delta P$, based on [8]. Hillis [8] differentiates between basin-scale PSC, demonstrated in the Scotian Shelf [11,12] or Brunei [9], and field-scale PSC, found in reservoirs in Texas [13], Venezuela [3] or the Ekofisk field in the North Sea [5]. Field-scale data, where PSC is measured to occur over a time scale of years during reservoir depletion, are obtained from approximately the same reservoir depth, whereas basin-scale date are collected over a range of depths and reflect the increase of pore pressure and stresses with depth. Therefore, the basin-scale data are depth-normalized in order to compare them with field-scale data. $\Delta\sigma_h/\Delta P$ varies between 0.34 and 1.18 with an average of 0.64.

Area	Scale	$\Delta\sigma_h/\Delta P$
Scotian shelf, Canada	Overpressure-related basin-scale	0.76
North West shelf, Australia	Overpressure-related basin-scale	0.75
Gannet and Guillemot fields, North Sea	Overpressure-related basin-scale	0.60
Vicksburg formation, South Texa	Depletion-related field-scale	0.48
Travis Peak formation, East Texas	Depletion-related field-scale	0.57
Alberta basin, Western Canada	Depletion-related field-scale	0.34
Ekofisk field, North Sea	Depletion-related field-scale	~0.8
US Gulf Coast	Depletion-related field-scale and overpressure-related basin-scale	0.46
Lake Maracaibo, Venezuela	Depletion-related field-scale	0.56
Baram Delta Province, Brunei	Depletion-related field-scale and overpressure-related basin-scale	0.59
Magnus field, North Sea	Depletion-related field-scale	0.68
West Sole field, North Sea	Depletion-related field-scale	1.18
Wytch Farm field, UK	Depletion-related field-scale	0.65
Venture field, Canada	Overpressure-related basin-scale	0.56
Nile Delta, Egypt	Overpressure-related basin-scale	0.65

induced microseismicity, phenomena that have profound impact on reservoir management [10,16]. Therefore, predictive geomechanical modelling of the reservoir's response to depletion or injection processes is an essential tool to forecast fluid flow and stress change within the reservoir and its surroundings [17].

Analytically, Engelder and Fischer [18] derive a space- and time-independent expression for the ratio $\Delta\sigma_h/\Delta P$ under the assumptions of (a) a horizontal infinitely large reservoir, (b) constant vertical stress σ_V, which is given by the overburden's weight and which does neither change laterally nor with changing pore pressure, (c) uniaxial strain condition with horizontal strains equal to zero and (d) equal changes in the maximum and the minimum horizontal stresses, $\Delta\sigma_H = \Delta\sigma_h$. They obtain

$$\frac{\Delta\sigma_h}{\Delta P} = \alpha\frac{1-2\nu}{1-\nu} \tag{1}$$

with the Biot–Willis coefficient α and the Poisson's ratio ν.

Numerical model computations, such as those reported in [19], show that the effective vertical stress changes quite significantly, and ascribe it to effects of the free-moving surface. Pore pressure drawdown during reservoir depletion results in reduced horizontal stresses within the reservoir. Conventionally this is ascribed to three different mechanisms: normal compaction, normal faulting and poroelasticity [20]. During sedimentation as well as during depletion sediments undergo normal compaction when the mean effective stress increases. The relationship between mean effective stress and porosity defines the so-called normal compaction curve. The normal faulting mechanism is based on the assumption that in a normal faulting regime there are critically stressed faults, which are optimally oriented for failure, and based on the Coulomb failure criterion the ratio of effective horizontal stress to effective vertical stress leads to a coupling coefficient [10,20], which depends on the coefficient of friction of the fault. This mechanism requires active faulting, which does not occur in sediments undergoing passive subsidence.

We focus on the poroelastic mechanism and thereby present the analytical solutions for the spatio-temporal pore pressure and stress evolution caused by continuous fluid injection/depletion at one point in homogeneous poroelastic infinite medium, derived by Rudnicki [21]. We use those analytical solutions to derive a space- and time-dependent ratio $\Delta\sigma_h/\Delta P\ (\boldsymbol{x}, t)$. In Section 3 we show that the ratio $\Delta\sigma_h/\Delta P\ (\boldsymbol{x}, t)$ results in Eq. (1), under consideration of the limit of infinite injection/depletion time. As Eq. (1) results from Rudnicki's equations [21] for $t \to \infty$, and thus represent a time-independent solution, we call it "long-term limit" in the following. This approach leads to an improvement in comparison to the conventional approaches, which are based on assumptions such as an infinite flat reservoir, constant vertical stress and zero horizontal strain [18].

As Rudnicki [21] describes the spatio-temporal distribution of the entire stress tensor, we are able to analytically investigate not only the coupling between P and σ_h, but between P and all stress components. Here, we concentrate on the coupling between P and the three normal stress components σ_{ii} $(i = 1, 2, 3)$. In particular, we analyse PSC ratios depending on the location with respect to the injection/depletion point, and on duration of injection/depletion. Using the finite element method, we numerically model the spatio-temporal evolution of pore pressure and stresses in poroelastic media induced by point injection into homogeneous three-dimensional space, and compare our modelling results to the analytical solutions [21,22] as well as to measured $\Delta\sigma_h/\Delta P$ data (Table 1). Furthermore, we analyse numerically the consequences of a higher permeable reservoir, which is embedded in surroundings with lower permeability on the spatio-temporal pore pressure and stress evolution, and thus on the PSC.

2. Poroelasticity equations

To derive the analytical stress and pore pressure solutions for continuous fluid injection into an infinite homogeneous poroelastic medium [21], we follow Wang [22]. The solutions are based on the Beltrami-Michell equations [(22), Eq. 4.27]

$$\nabla^2\sigma_{ij} + \frac{1}{1+\nu}\frac{\partial^2\sigma_{kk}}{\partial x_i\partial x_j} + 2\eta\left[\frac{1-\nu}{1+\nu}\frac{\partial^2 P}{\partial x_i\partial x_j} + \delta_{ij}\nabla^2 \mathrm{P}\right] = -\frac{\nu}{1-\nu}\delta_{ij}\vec{\nabla}\cdot\vec{F} - \frac{\partial F_i}{\partial x_j} - \frac{\partial F_j}{\partial x_i} \tag{2}$$

and on a pore pressure-mean stress equation [(22), eq. 4.63]

$$\frac{\alpha}{K_d B}\left[\frac{B}{3}\frac{\partial\sigma_{kk}}{\partial t} + \frac{\partial P}{\partial t}\right] - \frac{k}{\mu}\nabla^2 P = Q, \tag{3}$$

where the source term Q stands for the fluid source and describes the volume of fluid per unit bulk volume per unit time [22]. Eq. (2) stands for six coupled governing equations for the stress tensor σ_{kk}, which can be derived from the equations of equilibrium. σ_{kk} is the mean stress, ν the Poisson's ratio and η the poroelastic stress coefficient, which can be expressed by ν and the Biot-Willis coefficient a given by

$$\alpha = 1 - \frac{K_d}{K_g} \tag{4}$$

as

$$\eta = \frac{1-2\nu}{2(1-\nu)}\alpha \tag{5}$$

and Skempton's coefficient

$$B = \frac{3(\nu_u - \nu)}{\alpha(1+\nu_u)(1-2\nu)}. \tag{6}$$

The parameter K_d is denoted as drained bulk modulus, K_g as bulk modulus of the solid grains of the rock matrix and ν_u is the undrained Poisson's ratio. Eq. (3) is based on Darcy's law

$$\vec{q} = -\frac{k}{\mu}\vec{\nabla}\left(P + \rho_f g z\right) \tag{7}$$

which describes fluid flow through a porous medium. The fluid discharge crossing a unit area per unit time $\vec{q}$ [m/s] is related to the pressure gradient that is causing the fluid flow, k the permeability, μ the viscosity, ρ_f the fluid density and g the gravitational acceleration. Together with the continuity equation

$$\frac{\partial \xi}{\partial t} + \frac{\partial q_x}{\partial x} + \frac{\partial q_y}{\partial y} + \frac{\partial q_z}{\partial z} = Q \tag{8}$$

and the constitutive equation

$$\xi = \frac{\alpha}{K_d}\frac{\sigma_{kk}}{3} + \frac{\alpha}{K_d B}P \tag{9}$$

for the increment of fluid content ξ, Eq. (7) results in Eq. (3), which represents an inhomogeneous diffusion equation for the pore pressure. Solving Eq. (9) for σ_{kk} and substituting into Eqs. (2) and (3), and adding the two obtaining equations, one gets the diffusion equation

$$\frac{\partial \xi}{\partial t} = \frac{k}{\mu S}\nabla^2 \xi + \frac{k}{\mu}\frac{\lambda_u - \lambda}{\alpha(\lambda_u + 2G)}F_{k,k}, \tag{10}$$

with the drained and undrained Lamé parameters λ and λ_u, and the shear modulus G. The term $F_{k,k}$ is defined as

$$F_{k,k} \equiv \frac{\partial F_k}{\partial x_k}. \tag{11}$$

The Lamé parameters λ and λ_u can be expressed by G and the drained and undrained bulk moduli K_d and K_u, respectively

$$\lambda = K_d - \frac{2G}{3}, \tag{12a}$$

$$\lambda_u = K_u - \frac{2G}{3}. \tag{12b}$$

The undrained bulk modulus K_u can be written after Gassmann [23] as

$$K_u = \frac{K_g K_d\left(\varphi\left(K_g/K_f\right) - \varphi - 1\right)}{1 - \varphi - \left(K_d/K_g\right) + \varphi\left(K_g/K_f\right)}, \tag{13}$$

where φ is the porosity and K_f the bulk modulus of the wetting fluid.

Rudnicki [21] solves the differential equation of poroelasticity (Eq. (10)) and obtains for the spatio-temporal pore pressure and stress changes caused by continuous fluid injection at a point into infinite homogeneous poroelastic medium

$$P(\boldsymbol{x}, t) = \frac{q}{\rho_f c}\frac{1}{4\pi r}\left[\frac{(\lambda_u - \lambda)(\lambda + 2G)}{\alpha^2(\lambda_u + 2G)}\right]\operatorname{erfc}\left(\frac{1}{2}\xi\right), \tag{14}$$

$$\begin{aligned}\sigma_{ij}(\boldsymbol{x}, t) = -\frac{q}{\rho_f c}\frac{(\lambda_u - \lambda)G}{4\pi r\alpha(\lambda_u + 2G)}\Big\{\delta_{ij}\Big[\operatorname{erfc}\left(\frac{1}{2}\xi\right) \\ - \frac{2}{\xi^2}g(\xi)\Big] + \frac{x_i x_j}{r^2}\Big[\operatorname{erfc}\left(\frac{1}{2}\xi\right) + \frac{6}{\xi^2}g(\xi)\Big]\Big\},\end{aligned} \tag{15}$$

where q represents a constant-rate fluid mass source and ρ_f the fluid density, $\xi = r/\sqrt{ct}$ is the Boltzmann variable and c the diffusivity. The Lamé parameters under drained conditions are λ and G, whereas the undrained Lamé parameter is λ_u. $\operatorname{erfc}(z)$ represents the complementary error function of variable z; $\operatorname{erfc}(z)$ is connected to the error function $\operatorname{erf}(z)$ by $\operatorname{erfc}(z) = 1 - \operatorname{erf}(z)$, and the distance between pressure source (for injection $p > 40$, for depletion $q < 0$) and observation point is $|\boldsymbol{x}|$. In Eq. (15), we use the function

$$\begin{aligned}g(\xi) &= \frac{1}{2\sqrt{\pi}}\int_0^{\xi} s^2 \exp\left(-\frac{1}{4}s^2\right) ds \\ &= \operatorname{erf}\left(\frac{1}{2}\xi\right) - \frac{1}{\sqrt{\pi}}\xi\exp\left(-\frac{1}{4}\xi^2\right)\end{aligned} \tag{16}$$

From Eqs. (14) and (15), it is obvious that the pore pressure and stress changes are functions of the location with respect to the injection point and of the duration of injection, and depend on injection rate and permeability.

In the following the normal stress components σ_{xx}, σ_{yy} and σ_{zz} are analysed along the axes of a Cartesian coordinate system with its origin located at the injection point. Then, along the x-axis, for instance, σ_{xx} is radial stress and σ_{yy} and σ_{zz} are tangential stresses. Fig. 1 shows the possible combinations of radial and tangential stresses that occur along coordinate axes of a Cartesian coordinate system with the injection point at the origin of the coordinate system. Considering observation points along the horizontal x-axis, Eq. (15) yields for injection/depletion-induced radial and tangential stresses

$$\sigma_{xx}(\boldsymbol{x}, t) = \sigma_{rad}(\boldsymbol{x}, t) = -\frac{q}{\rho_f c}\frac{(\lambda_u - \lambda)G}{4\pi x\alpha(\lambda_u + 2G)}\Big[2\operatorname{erfc}\left(\frac{1}{2}\xi\right) + \frac{4}{\xi^2}g(\xi)\Big], \tag{17}$$

$$\begin{aligned}\sigma_{yy}(\boldsymbol{x}, t) = \sigma_{zz}(\boldsymbol{x}, t) = \sigma_{tan}(\boldsymbol{x}, t) \\ = -\frac{q}{\rho_f c}\frac{(\lambda_u - \lambda)G}{4\pi r\alpha(\lambda_u + 2G)}\Big\{\Big[\operatorname{erfc}\left(\frac{1}{2}\xi\right) - \frac{2}{\xi^2}g(\xi)\Big]\Big\}.\end{aligned} \tag{18}$$

The results for the spatio-temporal normal stress distribution as given in Eqs. (17) and (18) are valid for points on the horizontal x-axis with the injection point as origin of the coordinate system. However, considering a point located, for example, on the y-axis, the results for σ_{xx} and σ_{yy} exchange. In general, Eq. (17) describes the spatio-temporal changes in radial stress in radial direction, Eq. (18) describes the spa-

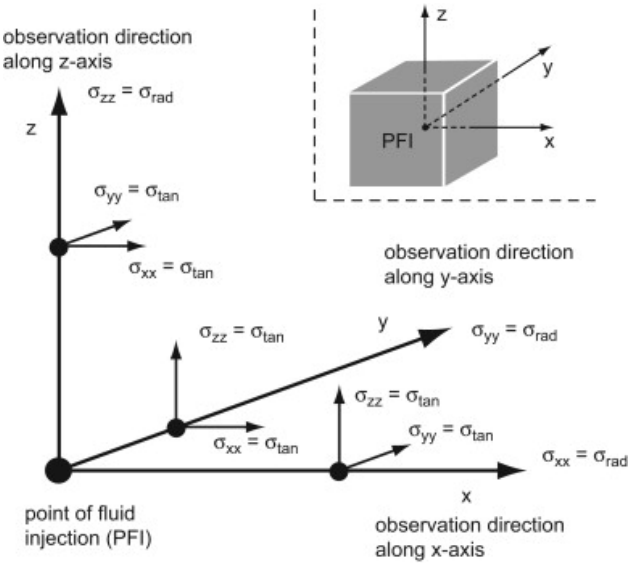

Figure 2. Pore pressure and stress changes are observed along the axes of a Cartesian coordinate system with its origin at the injection point. Then, the normal stress σ_{ii} along the i-axis ($i = x, y, z$) is radial stress, and the normal stress aii along the j-axis ($i, j = x, y, z;\ i \neq j$) is tangential stress.

tio-temporal changes in tangential stress, and Eq. (15) enables us to calculate stress states for arbitrary locations and times.

3. Pore pressure/stress coupling for long injection times

Based on Eqs. (14) and (15) the spatio-temporal evolution of PSC follows as

$$\frac{\Delta\sigma_{ij}(\boldsymbol{x},t)}{\Delta P(\boldsymbol{x},t)} = \frac{G\{\delta_{ij}[\mathrm{erfc}((1/2)\xi) - (2/\xi^2)g(\xi)] + (x_i x_j/r^2)[\mathrm{erfc}((1/2)\xi) + (6/\xi^2)g(\xi)]\}}{((\lambda+2G)/\alpha)\mathrm{erfc}((1/2)\xi)} \tag{19}$$

This equation is valid in case of injection and depletion. ΔP is the change in pore pressure in comparison to an initial pore pressure P_i. The total pore pressure is $P_{tot} = P_i + \Delta P$. In case of injection, ΔP is positive; in case of production, ΔP is negative. The stress change $\Delta\sigma_{ij}$ in comparison to the initial stress state σ_{ij} is associated with the change in pore pressure ΔP and derived directly from the formulae of Rudnicki [21].

Eq. (19) enables to calculate the spatio-temporal evolution of PSC for all stress components. In the following we consider the coupling between P and the normal stresses σ_{xx}, σ_{yy}, σ_{zz} along the axes of a Cartesian coordinate system with the origin at the injection/depletion point. According to radial and tangential stresses (Fig. 1), radial and tangential PSCs are calculated. For any radial stress component σ_{rad} (for i-j), and hence also the horizontal stress component σ_h, Eq. (19) simplifies to

$$\frac{\Delta\sigma_{rad}(\boldsymbol{x},t)}{\Delta P(\boldsymbol{x},t)} = \frac{2\alpha G}{\lambda+2G}\left\{1 + \frac{(2/\xi^2)g(\xi)}{\mathrm{erfc}(\xi/2)}\right\}. \tag{20}$$

According to [24]

$$\frac{2G}{\lambda+2G} = \frac{1-2\nu}{1-\nu}, \tag{21}$$

and so the difference between the time-dependent PSC ratio for radial stresses, Eq. (20), and the long-term limit solution, Eq. (1), depends on the spatio-temporal contribution of the second summand of Eq. (20). It can be shown using l'Hôpital's rule that for $\xi \to 0$, which represents either a zero distance to the origin, or an infinite injection time t

$$\lim_{t\to\infty} \frac{2g(\xi)}{\xi^2\mathrm{erfc}(\xi/2)} = 0. \tag{22}$$

Therefore, the PSC for infinite injection/depletion time is calculated, with usage of Eq. (21), as long-term limit

$$\lim_{t\to\infty} \frac{\Delta\sigma_{rad}(\boldsymbol{x},t)}{\Delta P(\boldsymbol{x},t)} = \alpha\frac{1-2\nu}{1-\nu}. \tag{23}$$

This demonstrates that the PSC based on the poroelastic relationships of Rudnicki [21] degenerates to Eq. (1) if time tends to infinity. As Engelder and Fischer [18] describe with Eq. (1) the coupling between pore pressure and minimum horizontal stress σ_h in reservoirs, Eqs. (1) and (23) are the same only if σ_h is radial stress. However, in comparison to the approach of [18], the boundary condition of zero horizontal strain has not to be used to derive Eq. (23). Analogously, the expression for the coupling between pore pressure and tangential stress is derived as

$$\lim_{t\to\infty} \frac{\Delta\sigma_{tan}(\boldsymbol{x},t)}{\Delta P(\boldsymbol{x},t)} = \frac{1}{2}\alpha\frac{1-2\nu}{1-\nu} = \frac{1}{2}\frac{\Delta\sigma_{rad}(\boldsymbol{x},t)}{\Delta P(\boldsymbol{x},t)}, \tag{24}$$

which is exactly half the value of the coupling of radial stress and pore pressure. In the following, the spatio-temporal PSC is investigated analytically. According to Eq. (19), PSC coefficients for both radial stress and tangential stress is calculated for different injection times and plotted versus distance to the injection point (Fig. 2), where the results are compared to measured field data. At the injection point both PSC ratios are identical with their long-term limit values. With increase in distance they diverge. For longer injection times, this divergence becomes smaller, and the PSC ratios are close to their long-term limits even for larger distances from the point source. For all injection times, a part of the radial PSC ratios is in the range of the measured field data, depending on location and duration of injection. Thus, the variability of the field data could be interpreted as a consequence of the different distances of the measurement location to the production wells and of different times since the beginning

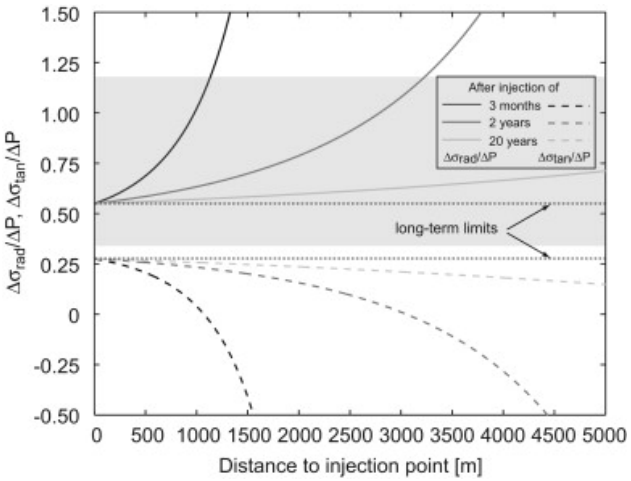

Figure 1. Spatio-temporal distribution of radial and tangential pore pressure/stress coupling ratios. Both, with duration of injection and with less distance to the injection point, radial and tangential PSC ratios approach their long-term limits. Directly at the injection point, the ratios are identical with their long-term limits, independent of injection time. The grey shaded area shows the range of measured field data (Table 1).

of production.

4. Numerical modelling of pore pressure and stress distribution

As Eqs. (14) and (15) are valid for a homogeneous isotropic poroelastic medium, which in general does describe neither the geological structure nor the material contrast between a reservoir and its surroundings, we use the finite element (FE) approach to model numerically the effect of fluid injection/depletion on the state of stress and the pore pressure distribution. From these results, we calculate with Eq. (19) the spatio-temporal evolution of PSC. First, we built a homogeneous 2D axis-symmetric FE-model with poroelastic material in order to verify our modelling results by comparison to the analytical solutions, Eqs. (14) and (15). This we can do as long as the pore pressure front has not reached the model boundary and no boundary effects have occurred to influence the result. To investigate the influence of an inhomogeneous permeability distribution we model in a second step an ellipsoidal reservoir with increased permeability, which is embedded in surroundings with lower permeability. For this approach we again use a 2D axis-symmetric FE-model. The partial pore pressure-stress differential equations are solved using the commercial software package ABAQUS/ Standard™ [25].

4.1. Model setup

Fig. 3 shows the setup of the 2D axis-symmetric FE-model. For both the homogeneous and the inhomogeneous approaches, we use the same model geometry. In the first case we assigned homogeneous material properties throughout the model. In the inhomogeneous case, we increased the permeability of an ellipsoid in 5 km depth, which should represent a reservoir. In Table 2 all input parameters required for the computation are listed. For both models the same material values are used, except of the permeability, which is increased by a factor of ten in the reservoir compared to the value of its surroundings, which is equivalent to the value of the homogeneous model. Those input parameters we also converted into parameters used by Rudnicki [21] in Eqs. (14) and (15), given in Table 3. The boundary conditions applied to the model are the same in both models. They are described by (a) a drained free surface at the top of the model, (b) undrained and in normal direction fixed model sides and model bottom, (c) an injection point located on the symmetry axis in a depth of 5 km, which in the case of the inhomogeneous model is located in the centre of the ellipsoid. The models consist of 46,477 continuum pore pressure quad elements with a maximal resolution of 7 m around the injection point, which decreases up to 900 m at the model boundaries. This enables us to model the spatio-temporal pore pressure and stress distributions generated by continuous fluid injection at one point over a large range, close to the injection point as well as in the far field.

4.2. Results, homogeneous model

Fig. 4 shows a comparison between modelled and analytically calculated pore pressure, normal stresses and PSC ratio distributions along the horizontal x-axis after 164 days of continuous fluid injection. Numerically calculated pore pressure and stress distributions (Fig. 4a) as well as PSC ratios (Fig. 4b) fit the analytical solutions. Close to the injection point pore pressure change ΔP is larger than the stress changes. With distance to the injection point ΔP decreases more strongly than the stress changes. This leads to an intersection point of the ΔP-profile with the $\Delta\sigma_{rad}$-profile. The location of this intersection point depends on the duration of injection. The tangential stress changes, i.e. $\Delta\sigma_{yy}$ and $\Delta\sigma_{zz}$ along the x-axis, even become slightly negative before converging towards zero with distance, this means that the induced stress change is tensile, which reduces the initial tangential stress. Despite of fluid injection and increase in pore pressure, it is possible that stresses also decrease. The

Table 2
Input parameters required for poroelastic modelling with ABAQUS. q_0 is the injected volume per time, ν the Poisson's ratio, e the void ratio, $k_{f,1}$ is the hydraulic conductivity of the homogeneous model and of the surroundings of the inhomogeneous model, $k_{f,2}$ is the hydraulic conductivity of the inner part of the inhomogeneous model.

q_0 (l/s)	ν	e	$k_{f,1}$ [10^{-6} m/s]	$k_{f,2}$ [10^{-6} m/s]	K_g (GPa)	K_f (GPa)	K_d (GPa)
20	0.3	0.2	0.1	1.0	40	2	12

Table 3
Material properties of the FE-model converted into values used in the analytical description, Eqs. (14) and (15) of [21]. The conversion itself and the formulae used for this process are shown in the Appendix.

q (kg/s)	ρ_f (kg/m³)	φ [1]	c (m²/s)	λ_u (GPa)	λ (GPa)	G (GPa)	α
20	1.000	0.167	0.082	13.4	8.3	5.5	0.7

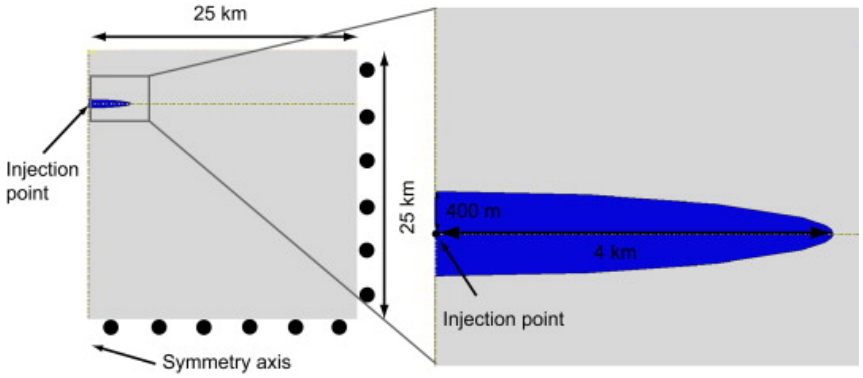

Figure 3. 2D axis-symmetric finite element model setup and boundary conditions used for the modelling of the spatio-temporal pore pressure and stress distributions caused by continuous fluid injection at one point. We applied poroelastic material properties to the model (Tables 2 and 3). In case of the inhomogeneous model, the permeability of the ellipsoidal reservoir is increased by a factor of ten. The injection point is located on the symmetry axis in 5 km depth.

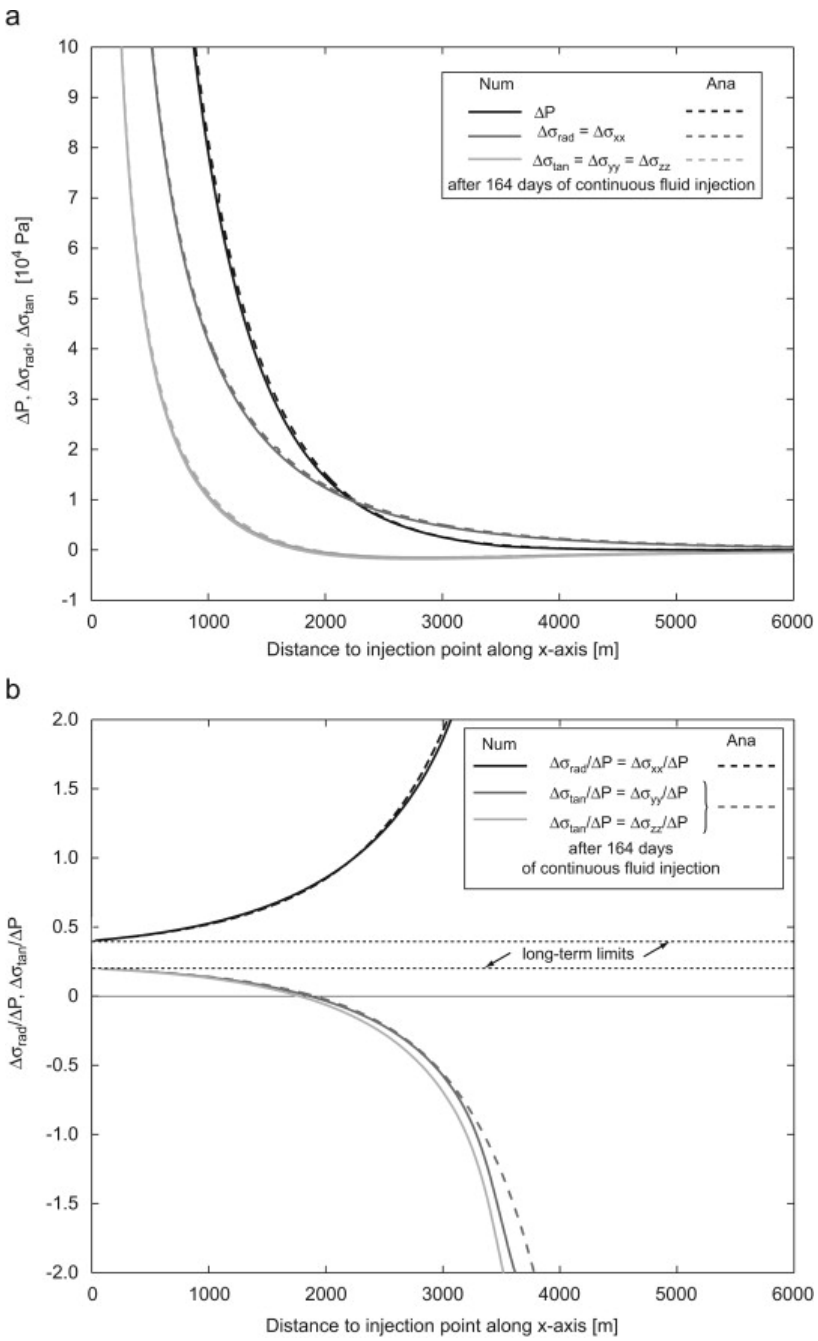

Figure 4. Results of the homogeneous modelling (solid curves) are shown here, which are compared to the analytical solutions (dashed curves). (a) the spatial distribution of pore pressure and normal stress changes along the x-axis. (b) the PSC ratios, both after 164 days of fluid injection. In both sub-figures modelled and analytical results are compared to one another. In subfigure (b) the theoretical values of radial and tangential PSC long-term limits are drawn as horizontally dotted lines.

analytical long-term limits of 0.4 for the radial PSC ratio and of 0.2 for the tangential one, according to Eq. (1), are modelled with our numerical approach. The numerical results fit those values at the injection point, and diverge with increase in distance from the point source. The radial PSC ratio increases, whereas the tangential PSC ratios decrease. This diverging behaviour of both PSC ratios is due to the fact that ΔP converges more strongly towards zero than the stress changes do. Therefore, the ratio $\Delta\sigma/\Delta P$ goes to $+\infty$ (radial component) and $-\infty$ (tangential components), with increase in distance to the injection point. The tangential PSC ratios $\Delta\sigma_{yy}/\Delta P$ and $\Delta\sigma_{zz}/\Delta P$ along the x-axis differ between each other. This is due to a boundary effect. In the analytical approach, a point injection into infinite poroelastic medium is considered, whereas in our modelling approach, the infinite medium is realized by model boundaries far away from the injection point to avoid boundary effects. The drained free top surface is the model boundary with the least distance to the injection point. Therefore, it influences the pore pressure and stress distribution for longer injection times, when pore pressure has diffused to the model boundary. As the free surface will move mainly in vertical direction during fluid injection, it mostly will affect the vertical stress change $\Delta\sigma_{zz}$, and thus the PSC ratio $\Delta\sigma_{zz}/\Delta P$.

4.3. Results, inhomogeneous model

The higher permeable inner part of the inhomogeneous model causes pore pressure to diffuse faster inside the res-

ervoir, so that pore pressure is not able to build up that much than in the homogeneous case. This leads to decreased pore pressure and stress changes inside the ellipsoidal reservoir compared to the results of the homogeneous model. Fig. 5a and b shows the spatio-temporal evolution of P and stress changes along the x-axis. Comparing to the homogeneous modelling results (Fig. 4), it clearly can be seen that pore pressure and stress changes are smaller inside the ellipsoidal reservoir. The decreased permeability outside the reservoir ($x \geq 4000$ m) retards the pore pressure to diffuse as fast as inside the reservoir. This leads to a stronger decrease of ΔP inside the surroundings (Fig. 5a). For longer injection times (Fig. 5b), ΔP is diffused wider, so that ΔP decreases less strong at the reservoir-surroundings boundary.

In general, the stress distribution is not influenced by the permeability contrast like the pore pressure distribution, because the stresses are transferred via the rock frame, and permeability describes the ability of fluid diffusion through the pore spaces. Thus, in the surroundings stress decreases less strong than P. The different diffusion character of stress and P leads to an increase (radial component) or decrease (tangential components) of PSC values inside the surroundings. With duration of injection ΔP also spreads out in the surroundings, so that the effect of strong increasing PSC ratios at the reservoir-surroundings boundary diminishes. The tangential stresses $\Delta\sigma_{zz}$ and $\Delta\sigma_{zz}$ are different, because of the effect of the free surface. As the model surface is not constrained, it can move with the pore pressure and the stresses building up due to fluid injection. As the movement mainly occurs in vertical direction, the vertical stress change $\Delta\sigma_{zz}$ is affected most by the free surface, and thus also the PSC ratio $\Delta\sigma_{zz}/\Delta P$. As the free surface is moving upward during fluid injection, stresses increase less than in the cases of an infinite medium or a model with the surface constrained to move. Therefore, $\Delta\sigma_{zz}$ and $\Delta\sigma_{zz}/\Delta P$ are smaller than the other tangential stress $\Delta\sigma_{zz}$ and PSC ratio $\Delta\sigma_{zz}/\Delta P$ (Fig. 5).

The shape of the ellipsoidal reservoir also influences the pore pressure and the PSC ratio distribution. Close to the reservoir-surroundings boundary, the ellipsoidal reservoir is narrowing and in all directions surrounded by less permeable material. In this part of the reservoir, fluid diffusion is retarded, and thus pore fluid is retained inside the reservoir close to the surroundings. Additional fluid leads to less decreasing ΔP values (Fig. 5a) with distance to the injection point or even to a slightly increasing ΔP (Fig. 5b) for $3500 \leq x \leq 4000$ m. Less decreased or increased ΔP, respectively, leads to decreased PSC values in this area (Fig. 5c and d).

4.4. Comparison with measured field-data

In the following, we compare our modelling results with the measured field data. Fig. 6 shows that our modelled PSC ratios are in the range of the measured field data, for short as well as for long injection times, and close to the injection point as well as in the far field. As our modelling results show, the variation in the measured field data could be caused by different time periods between start of injection and measurement, by different distances between meas-

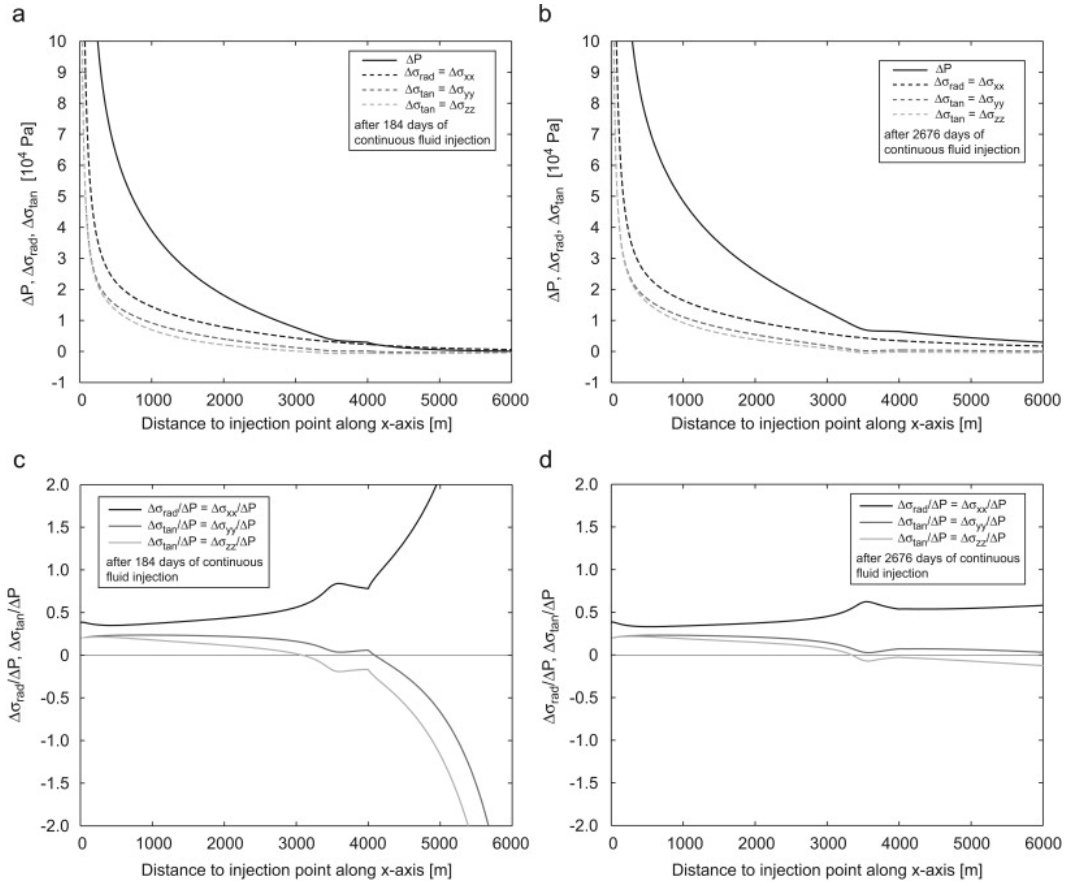

Figure 5. (a–d) show results derived from the pore pressure and stress modelling using the inhomogeneous model setup. Displayed are the spatial distributions of pore pressure and stress along the x-axis after injection times of 184 days (a) and 2676 days (b) $\Delta\sigma_{xx}$. $/\Delta P$, $\Delta\sigma_{yy}/\Delta P$ and $\Delta\sigma_{zz}/\Delta P$ distributions along the x-axis are provided in (c) for 184 days and (d) for 2676 days of injection. Due to the faster diffusion of pore pressure inside the reservoir, already after short injection times a kind of steady state for pore pressure and stress is reached with only less increasing values inside the reservoir area.

urement location and injection source and by the measurement location with respect to the injection source and the stress field. The latter point means that at one location the measured minimum horizontal stress is the radial stress, at another location the tangential stress, which both differ clearly (Figs. 4 and 5).

5. Discussion

The pore pressure induced change of radial stress for injection and depletion are different in comparison to the tangential stresses. For example along the x-axis, σ_{xx} is twice the value of σ_{yy} and σ_{yy}. This leads to different PSC ratios for vertical and horizontal stresses. The consequences of the tensor character of pore pressure/stress coupling based on the analytical computations are discussed in detail [26]. Here we consider the effects of pore pressure/stress coupling in numerical reservoir models. We first compare for simple geometries the analytical solution with the numerical results of a fully coupled poroelastic finite element model and obtain identical graphs for σ_{yy} and σ_{yy} (Fig. 4a), for both the analytical and numerical results. Pore pressure and stress changes depend on injection rate and material properties of our model. But, pore pressure and stresses vary also as a function of locality and time for constant injection rate and material properties.

We interpret the increase in the PSC ratio with distance to the injection point to results from the fact that the stress change is transferred through the granular structure whereas the pore pressure change is diffusing. Thus, the stress change increases faster with distance than the pore pressure change. Since the pore pressure change is higher at the injection point than the stress change, there is an intersection point of pore pressure and stress changes at a certain distance from the injection point, which depends on the injection time (Fig. 4a). In the homogeneous model, there are minor deviations between numerical results and analytical solutions (Fig. 4), which we interpret to be attributed to the finite model size, the undrained and in normal direction fixed model side and model bottom and the drained and free model top surface.

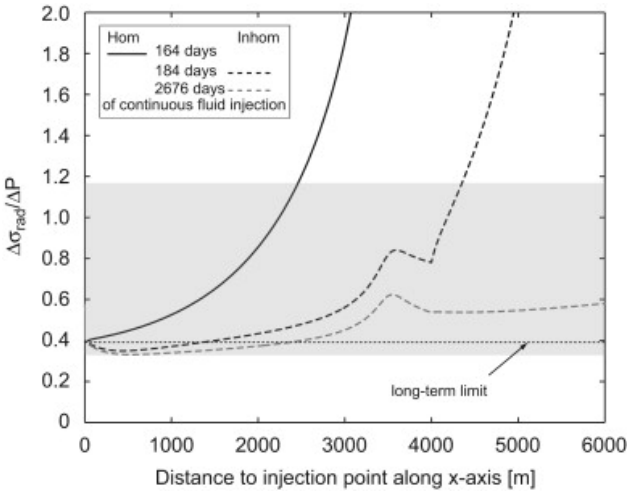

Figure 6. Comparison of numerical modelling results for three injection times in homogeneous and inhomogeneous poroelastic medium with the analytical long-term limit (horizontally dotted line) of the radial PSC and the range of measured field-data (grey shaded area). At the injection source, all numerical values are identical with the long-term limit value. For longer injection times and in the case of a higher permeable reservoir, PSC values are closer to the long-term limit also at larger distances to the injection point.

In the inhomogeneous model within the high-permeability zone fluid flows fast towards the surroundings, which leads to a smaller build-up of pore pressure and via coupling stress changes inside the higher permeable part in comparison to the homogenous model. The spatio-temporal PSC ratio is shown in Fig. 5c and d. There is a reduction in PSC within the inner part in comparison to the values of the homogeneous model and an increase in PSC at the boundary between inner and outer parts. The reason for this increase is that in the less permeable surroundings the pore pressure cannot diffuse as fast as inside the higher permeable inner part, and converges in the surroundings much faster towards zero than the stress does. Since the PSC at the ''reservoir'' boundary can reach values of 0.6 even for longer injection/production times, this means, that stress changes in the order of 60% of pore pressure change within a reservoir occur at the reservoir boundaries, which might, for example, affect the stability of reservoir bounding faults. Close to the injection point the PSC ratios are close to the long-term limit solution, independent of the injection time. With distance to the injection point the radial stress ratio $\Delta\sigma_h/\Delta P$ increases strongly with distance. However this increase diminishes for longer injection times, i.e. for infinite injection time – equivalent to the long-term solution – the modelled $\Delta\sigma_h/\Delta P$ distribution would fit the long/term solution.

Depending on injection time and distance to the injection point, the modelled values are in the range of the measured field-data. With the concept of poroelasticity it is possible to explain the measured (Table 1) PSC ratios. Different values of this ratio would result from different locations with respect to the injection point and/or different injection times. Only for long injection times the PSC values approach the long-term limit solution. Otherwise this value is reached only in the vicinity of the injection point. The variation in the measured PSC ratios in different oil fields can be explained by the distance to the injection point and the time since start of injection.

6. Conclusions, outlook

We conclude that pore pressure/stress coupling is not a constant value throughout the lifetime of a reservoir and varies within the reservoir as a function of distance to the producing/injecting wells and of time since begin of production/injection. We show analytically that the uniaxial strain approach [18] can be deduced as long-term limit of the poroelastic equations. We also showed that the normal stress components differ in their PSC ratios. Both, the analytical and our modelling results indicate that the pore pressure/stress coupling deviates at reservoir scale from the long-term limit in particular during the first months of injection or depletion, or for larger distances from the injection point. Only for distances close to the injection point and for long injection times the long-term limit for the pore pressure/stress coupling is obtained. Therefore we conclude that the measured variations in PSC ratios can be explained, e.g., by the variation in depletion rates, time since depletion started and well position within the reservoir.

Our modelling studies have shown the importance of the reservoir shape and the permeability changes at the reservoir boundaries. The results of the inhomogeneous model indicate that reservoir shape as well as the contrast of material properties between the reservoir and the surroundings may control the distribution of pore pressure and stress, and thus pore pressure/stress coupling. Stress changes in the order of 60% of the pore pressure changes are to be expected at reservoir boundaries. For short injection/production times the values could be much higher. The poroelastic

finite element modelling enables us to calculate pore pressure, the normal stress σ_n and the shear stress τ as a function of time for any location. As a perspective, these fields can be included in a failure criterion for shear and tensile failure to predict the spatio-temporal distribution of failure planes either for fracturing or for reactivation of pre-existing fractures [27].

Acknowledgments

This research has been supported by the Heidelberg Academy of Sciences and Humanities, the sponsors of the consortium project PHASE and the Deutsche Forschungsgemeinschaft (MU1725/1-3). We thank one anonymous reviewer and Peter Schutjens for the constructive comments.

Appendix

Calculation of material parameters used in Eqs. (14) and (15) from variables required and specified for the numerical modelling with ABAQUS. Those input parameters are (variable set A) the injection rate q_0, Poisson's ratio ν, void ratio e, hydraulic conductivity k_f, bulk moduli K_g of solid grains and K_f of the wetting fluid and the drained bulk modulus K_d.

The variables specified in Eqs. (14) and (15) for the calculation of the spatio-temporal P and stress distributions after continuous point injection, are (variable set B): the injected fluid mass per time q, the fluid density ρ_f, the porosity φ, the Biot–Willis coefficient α, the undrained Lamé parameter λ_u, and the drained Lamé parameters λ, G and the diffusivity, c.

The variable set B can be calculated by means of variable set A as follows:

$$q = q_0 \rho_f \tag{A1}$$

$$\varphi = \frac{e}{1+e} \tag{A2}$$

$$G = 3K_d \frac{1-2\nu}{2+2\nu} \tag{A3}$$

The coefficient α and the Lamé parameters are calculated using Eqs. (4), (12a), (12b) and (13), after which the diffusivity c can be calculated by

$$c = \frac{k(\lambda_u - \lambda)(\lambda + 2G)}{\alpha^2(\lambda_u + 2G)} \tag{A4}$$

with

$$k = \frac{k_f}{g\rho_f}, \tag{A5}$$

where g is the gravitational acceleration.

References

[1] Hillis RR. Coupled changes in pore pressure and stress in oil fields and sedimentary basins. Pet Geosci 2001;7:419–25.

[2] Addis MA. The stress-depletion response of reservoirs. In: Proceedings of the SPE Annual Technology Conference and Exhibition, 5-8 Oct 1997, San Antonio, paper SPE 38720.

[3] Breckels IM, van Eekelen HAM. Relationship between horizontal stress and depth in sedimentary basins. J Pet Technol 1982;34:2191-8.

[4] Addis MA. Reservoir depletion and its effect on wellbore stability evaluation. Int J Rock Mech Min Sci 1997;34(3-4). paper 004.

[5] Teufel L, Rhett D, Farrell H. Effect of reservoir depletion and pore pressure drawdown on in situ stress and deformation in the ekofisk field, north sea. In: Roegiers JC, editor. Rock mechanics as a multidisciplinary science. Rotterdam: Balkema; 1991. p. 63–72.

[6] Teufel LW. Influence of pore pressure and production-induced changes in pore pressure on in-situ stress. SANDIA report SAND96-0534 UC-132, Sandia Nat Lab, Albuquerque, 1996. 54 pp.

[7] Santarelli FJ, Tronvoll JT, Svennekjaier M, Skeie H, Henriksen R, Bratli RK. Reservoir stress path: the depletion and the rebound. In: Proceedings of the SPE/ISRM Conference on Rock Mechanics and Petroleum Engineering, Trondheim, 1998. paper SPE 47350.

[8] Hillis RR. Pore pressure/stress coupling and its implications for seismicity. Explor Geophys 2000;31:448–54.

[9] Tingay MRP, Hillis RR, Morley CK, Swarbrick RE, Okpere EC. Pore pressure/ stress coupling in Brunei Darussalam - implications for shale injection. In: von Rensbergen P, Hillis RR, Maltman AJ, Morley CK, editors. Subsurface sediment mobilization. London: Geological Society; 2003. p. 369–79.

[10] Zoback M, Zinke J. Production-induced normal faulting in the valhall and ekofisk oil fields. Pure Appl Geophys 2002; 159:403–20.

[11] Bell JS. The stress regime of the Scotian Shelf offshore eastern Canada to 6 kilometers depth and implications for rock mechanics and hydrocarbon migration. In: Maury V, Fourmaintraux D, editors. Rock at great depth. Rotterdam: Balkema; 1990. p. 1243–65.

[12] Ervine WB, Bell JS. Subsurface in situ stress magnitudes from oil-well drilling records: an example from the Venture area, offshore eastern Canada. Can J Earth Sci 1987;24:1748–59.

[13] Salz LB. Relationship between fracture propagation pressure and pore pressure. In: Proceedings of the SPE Annual Technical Conference and Exhibition, 9–12 Oct 1977, Denver. Paper SPE 6870.

[14] Roest JPA, Mulders FMM, Kuilman W. Data-limited geomechanical modelling for investigating induced seismicity mechanisms. In: Proceedings of the 9th International Congress on Rock Mechanics, Paris, 1999. p 1061–4.

[15] Mulders F.M.M. Modelling of stress development and fault slip in and around a producing gas reservoir. Thesis, Tech Univ Delft, 2003. p. 272.

[16] Schutjens PMTM, Burrell R, Fehmers G, Hindriks K, Collins C, van der Horst J. On the stress changes in overburden resulting from reservoir compaction: Observations from two computer models and implications for 4d seismic. Leading Edge 2007;26:628–34.

[17] Settari A, Walters DA. Advances in coupled geomechanical and reservoir modelling with application to reservoir compaction. SPE J 2001;3(6):334–42.

[18] Engelder T, Fischer MP. Influence of poroelastic behaviour on the magnitude of minimum horizontal stress, Sh, in overpressured parts of sedimentary basins. Geology 1994;22: 949-52.

[19] Rutqvist J, Birkholzer J, Cappa F, Tsang C-F. Estimating maximum sustainable injection pressure during geological sequestration of CO2 using coupled fluid flow and geomechanical fault-slip analysis. Energy Convers Manage 2007; 48:1798–807.

[20] Goulty N. Reservoir stress path during depletion of norwegian chalk oil fields. Pet Geosci 2003;9:233–41.
[21] Rudnicki JW. Fluid mass sources and point forces in linear elastic diffusive solids. Mech Mater 1986;5:383–93.
[22] Wang HF. Theory of linear poroelasticity. Princeton: Princeton University Press; 2000.
[23] Gassmann F. Ueber die Elastizitaet poroeser Medien. Vierteljahrschrift Naturforsch Ges Zuerich 1996;96:1–23.
[24] Jaeger JC, Cook NGW, Zimmerman RW. Fundamentals of rock mechanics. 4th edition. Oxford: Wiley-Blackwell; 2007.
[25] ABAQUS, Inc. (2004). ABAQUSTM, ABAQUS Version 6.5 Documentation.
[26] Müller B, Altmann JB, Müller TM, Weisshardt A, Shapiro SA, Schilling F, Heidbach O. Tensor character of pore pressure-stress coupling in reservoir depletion and injection. 72nd EAGE Conference, Barcelona, 2010. Extended abstracts F045.
[27] Rozhko AY, Podladchikov YY, Renard F. Failure patterns caused by localized rise in pore-fluid overpressure and effective strength of rocks. Geophys Res Lett 2007; 34:L22304.